The Astrophysical Journal, 636:323–331, 2006 January 1

SUBMILLIMETER ARRAY 440 μm/690 GHz LINE AND CONTINUUM OBSERVATIONS OF ORION KL

H. Beuther,[1,2] Q. Zhang,[1] M. J. Reid,[1] T. R. Hunter,[1] M. Gurwell,[1] D. Wilner,[1] J.-H. Zhao,[1]
H. Shinnaga,[1] E. Keto,[1] P. T. P. Ho,[1] J. M. Moran,[1] and S.-Y. Liu[3]
Received 2005 July 8; accepted 2005 September 12

ABSTRACT

Submillimeter Array observations of Orion KL at $\sim 1''$ resolution in the 440 μm/690 GHz band reveal new insights about the continuum and line emission of the region. The 440 μm continuum flux density measurement from source *I* allows us to differentiate among the various proposed physical models. Source *I* can be well modeled by a "normal" protostellar spectral energy distribution (SED) consisting of a proton-electron free-free emission component at low frequencies and a strong dust component in the submillimeter bands. Furthermore, we find that the protostellar object SMA1 is clearly distinct from the hot core. The nondetection of SMA1 at centimeter and infrared wavelengths suggests that it may be one of the youngest sources in the entire Orion KL region. The molecular line maps show emission mainly from source *I*, SMA1, and the hot core peak position. An analysis of the $CH_3CN(37_K–36_K)$ *K*-ladder ($K = 0, \ldots, 3$) indicates a warm gas component of the order of 600 ± 200 K. In addition, we detect a large fraction ($\sim$58%) of unidentified lines and discuss the difficulties of line identification at these frequencies.

Subject headings: ISM: individual (Orion KL) — ISM: lines and bands — ISM: molecules — stars: formation — submillimeter — techniques: interferometric

1. INTRODUCTION

The 440 μm/690 GHz band is almost entirely unexplored at high spatial resolution. In 2005 February, the Submillimeter Array (SMA)[4] performed the first imaging campaign in that band with six antennas in operation; thus, line and continuum imaging at $1''$ resolution was possible at frequencies around 690 GHz. One of the early targets of this campaign was the Orion KL region.

At a distance of $\sim$450 pc, Orion KL is the closest and most studied region of massive star formation in our Galaxy. Furthermore, the Orion KL hot core is known to be particularly rich in molecular line emission (e.g., Wright et al. 1996; Schilke et al. 2001; Beuther et al. 2005). The hot core as traced by (sub)millimeter dust continuum emission is a chain of clumps offset by $\sim 1''$ from radio source *I*. The hot core is rich in nitrogen-bearing molecules such as CH_3CN and NH_3 and has temperatures of the order of a few hundred kelvins (e.g., Wilner et al. 1994; Wilson et al. 2000; Beuther et al. 2005). In contrast, the so-called compact ridge approximately $5''$ to the south is particularly rich in CH_3OH emission and has lower temperatures of the order of 100 K (e.g., Wright et al. 1996; Liu et al. 2002; Beuther et al. 2005). In addition, the region harbors a complex cluster of infrared sources studied in from near- to mid-infrared wavelengths (e.g., Dougados et al. 1993; Gezari et al. 1998; Greenhill et al. 2004; Shuping et al. 2004). At least two outflows are driven from the region, one high-velocity outflow in the southeast-northwest direction (e.g., Allen & Burton 1993; Chernin & Wright 1996; Schultz et al. 1999), and one lower velocity outflow in the northeast-southwest direction (e.g., Genzel & Stutzki 1989; Blake et al. 1996; Chrysostomou et al. 1997; Stolovy et al. 1998; Beuther et al. 2005). The driving source(s) of the outflows are uncertain. Initial claims that it might be IRc2 are outdated now, and possible culprits are radio source *I* and/or infrared source *n*, also known as radio source *L* (Menten & Reid 1995).

In 2004, we observed Orion KL at $1''$ resolution with the SMA in the 865 μm/348 GHz band (Beuther et al. 2004, 2005). The molecular line data show a rich line forest resolving different spatial structures for the various species. The SiO(8–7) observations convincingly show that the northeast-southwest outflow emission originates at source *I*. Temperature estimates based on a CH_3OH multiline fit result in values as high as 350 K for the hot core. In the 865 μm submillimeter continuum data, source *I* was resolved from the hot core and source *n* was detected as well. The spectral energy distribution of source *I* from 8 to 348 GHz still allowed ambiguous interpretations of its physical nature (see also § 3.1.3). Furthermore, a new continuum peak, SMA1, between sources *I* and *n* was detected; however, the nature of SMA1 was uncertain, as it could have been either an independent protostellar core or part of the extended hot core. In this paper, our new observations in the 440 μm band clarify the natures of SMA1 and source *I*.

2. OBSERVATIONS

We observed Orion KL with the SMA on 2005 February 19 in the 440 μm/690 GHz band. Six antennas were equipped with 690 GHz receivers, and the covered baselines ranged between 16 and 68 m. The weather conditions were excellent with a zenith opacity—measured with the National Radio Astronomy Observatory (NRAO) tipping radiometer located at the Caltech Submillimeter Observatory—of τ(230 GHz) between 0.03 and 0.04 throughout the night. This corresponds to zenith opacities at 690 GHz between 0.6 and 0.8 [τ(690 GHz) $\sim 20[\tau(230\ \mathrm{GHz}) - 0.01]$; Masson 1994]. The phase center was the nominal position of source *I* as given by Plambeck et al. (1995): R.A. (J2000.0) = $5^h35^m14^s.50$ and decl. (J2000.0) = $-5°22'30''.45$. The FWHM of the primary beam of the SMA at these frequencies is $18''$, and

[1] Harvard-Smithsonian Center for Astrophysics, 60 Garden Street, Cambridge, MA 02138; hbeuther@cfa.harvard.edu.
[2] Max-Planck-Institut für Astronomie, Königstuhl 17, 69117 Heidelberg, Germany; beuther@mpia.de.
[3] Academia Sinica Institute of Astronomy and Astrophysics, National Taiwan University, 1 Roosevelt Road, Section 4, Taipei 106, Taiwan.
[4] The Submillimeter Array is a joint project between the Smithsonian Astrophysical Observatory and the Academia Sinica Institute of Astronomy and Astrophysics and is funded by the Smithsonian Institution and the Academia Sinica.

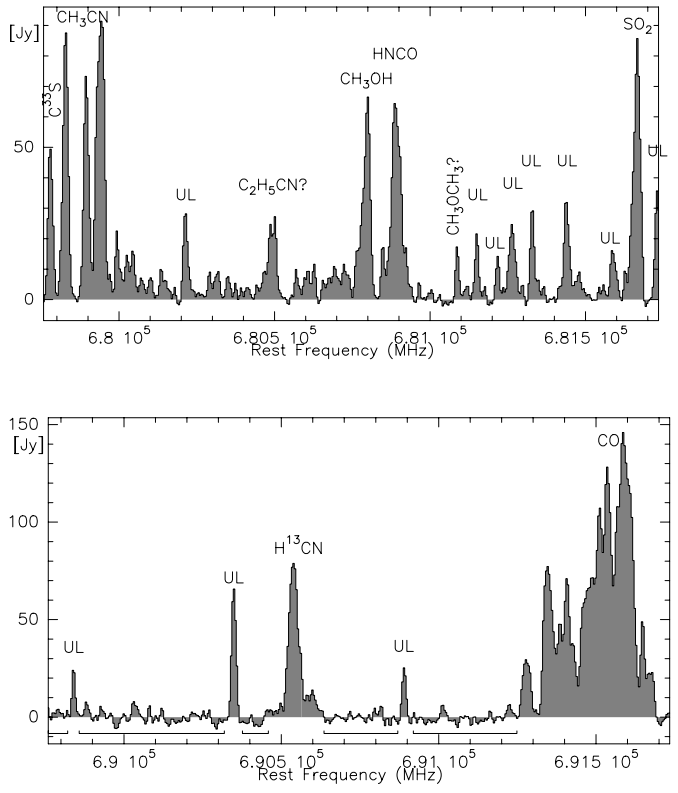

FIG. 1.—Vector-averaged lower and upper sideband spectra in the *u-v* domain on a baseline of ~25 m. The data are averaged over an hour angle range from −2^h.6 to +4^h.5 with a total on-source integration time of 176 minutes. "UL" marks unidentified lines and "?" marks tentatively identified lines. The lines at the bottom of the upper sideband spectrum mark the apparently line-free part of the spectrum, which we used to produce the 440 μm continuum image (Figs. 3 and 4).

the aperture efficiency is ~0.4. For more details on the array and its capabilities, see Ho et al. (2004).[5]

The receivers operated in a double-sideband mode with an intermediate-frequency (IF) band of 4–6 GHz so that the upper and lower sidebands were separated by 10 GHz. The correlator had a bandwidth of 1.968 GHz, and the channel spacing was 0.8125 MHz. The covered frequency ranges were 679.78–681.75 and 689.78–691.75 GHz (Fig. 1). Bandpass calibration was done with observations of Callisto (angular diameter ~1.″4). Since no quasar is strong enough in that band for calibration purposes, we calibrated phase and amplitude via frequent observations of Titan (angular diameter ~0.″9). The distances of Callisto and Titan from Jupiter and Saturn were >230″ and ~190″, respectively. The contamination of the Callisto and Titan fluxes by their primaries is negligible for mainly three reasons: (1) the primary beam pattern severely attenuates these planets, since they are much more than 10 primary beams away, (2) the large size of the planets (40″ for Jupiter, 20″ for Saturn) implies that a large fraction of their fluxes is resolved out, and (3) due to the motion of the moons over the period of observation, any small contamination will not be added coherently, further reducing the contamination issue.

The large angle between Titan and Orion KL (~40°) introduced larger than normal uncertainties in the phase and amplitude transfer. The flux calibration was performed with the Titan observations as well, for which a well-calibrated model has been created and used extensively at millimeter wavelengths (Gurwell & Muhleman 1995, 2000; Gurwell 2004). In the current observations, the upper sideband (USB) included the CO(6–5) line, which is quite broad as determined by using both observations of lower CO transitions and modeling of the expected line shape, assuming that CO has a uniform 50 ppm (parts per million) abundance in the Titan atmosphere (Gurwell 2004). Modeling the flux of the continuum lower sideband (LSB) and continuum + CO(6–5) USB emission, the expected average Titan fluxes at the given dates were 12.0 and 22.3 Jy for the LSB and USB, respectively. Based on flux measurements of the two main continuum sources in Orion KL using only the part of the spectra with no detectable line emission (§ 3.1), we estimate the relative flux accuracy between the USB and LSB to be better than 10%. The absolute flux calibration was estimated to be accurate within ~25%.

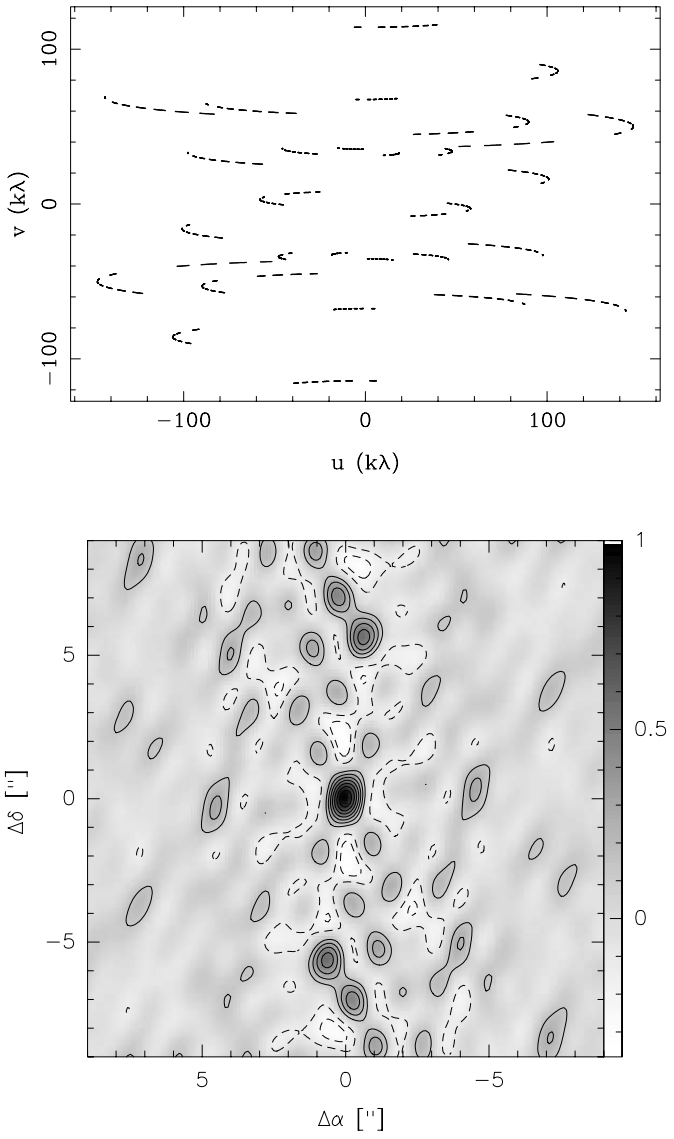

FIG. 2.—*Top:* The *u-v* coverage of the observations. *Bottom:* Resulting dirty beam; contour levels cover the range ±1, in steps of ±0.125.

Since Orion KL is close to the celestial equator, and since we have for most baselines only source data observed in an hour angle range from −2^h.6 to +1^h.2 (the data of only three baselines were usable over a longer range from −2^h.6 to +4^h.5), imaging of the data proved to be difficult. Figure 2 shows the given *u-v* coverage and the resulting dirty beam. In spite of the large-scale emission present in Orion KL, we had to employ clean boxes covering the central region around source *I*, SMA1, and the main hot core

[5] Recent updates are given at http://sma1.sma.hawaii.edu/specs.html.

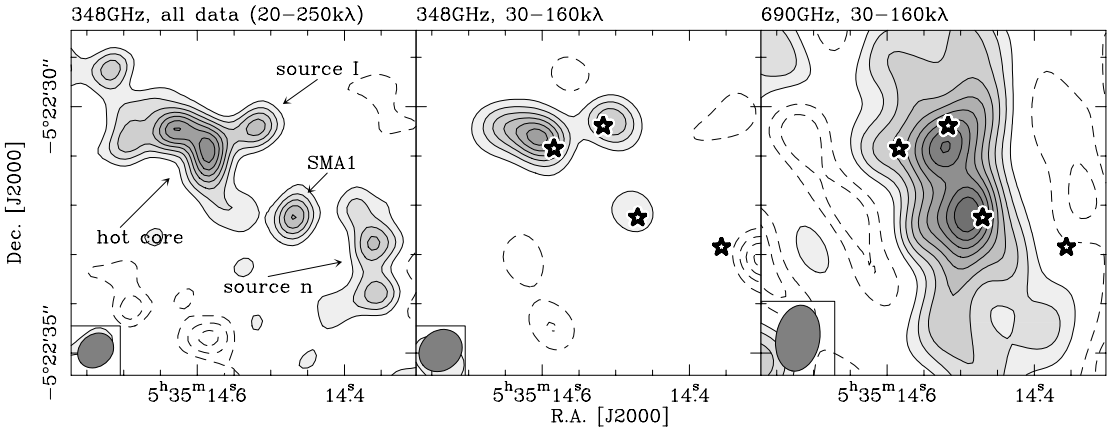

FIG. 3.—Submillimeter continuum images of Orion KL. Positive emission is shown in a gray scale with contours; negative features—due to missing short spacings and the calibration/imaging difficulties discussed in § 2—are presented in dashed contours. *Left:* Previously published 348 GHz continuum data (Beuther et al. 2004). The contours start at the 2 σ level of 70 mJy beam^{-1} and continue in 2 σ steps. The main sources in the region are labeled by name. *Middle:* Image of the same region, with a limited range of *u-v* data between 30 and 160 kλ. The contouring is the same as in the left panel, and the stars mark the four sources identified in the left panel. *Right:* New 690 GHz continuum data covering a *u-v* range between 30 and 160 kλ again (blanking the only bin below 30 kλ at 28 kλ). The contouring is done in 10%–90% steps from the peak emission of 10.3 Jy, and the stars again mark the sources identified in the left panel. The synthesized beams are presented at the bottom left of the panels. The different synthesized beams in the middle and right panels result from a different *u-v* sampling, although we applied the same *u-v* limits.

peak to derive reasonable images because of the high sidelobe levels. Measured double-sideband system temperatures corrected to the top of the atmosphere were between 900 and 3500 K, depending on the elevation of the source. Our sensitivity was limited by the strong sidelobes of the strongest emission peaks and thus varied between the continuum and the line maps of different molecules and molecular transitions. This limitation was mainly due to the incomplete sampling of short *u-v* spacings and the presence of extended structures. The achieved 1 σ rms of the 440 μm continuum image, produced by averaging the apparently line-free part of the USB spectrum (see § 3.1), was $\sim$700 mJy beam^{-1}—well above the expected 1 σ of $\sim$41 mJy beam^{-1} for the given on-source time, the used bandpass, and an average τ(230 GHz) = 0.037 (corresponding to 0.61 mm precipitable water vapor). This larger rms was mainly due to the strong sidelobes and inadequate cleaning. The theoretical 1 σ rms per 1 km s^{-1} channel was $\sim$775 mJy beam^{-1}, whereas the measured 1 σ rms in the 1 km s^{-1} channel images was $\sim$2.6 Jy beam^{-1}, again because of the strong sidelobes and inadequate cleaning. The 1 σ rms for the velocity-integrated molecular line maps (the velocity ranges for the integrations were chosen for each line separately depending on the line widths and intensities) ranged between 1.1 and 1.6 Jy beam^{-1}. The synthesized beams were $1\farcs4 \times 0\farcs9$ using an intermediate weighting between natural and uniform ("robust" value 0 in MIRIAD). We calibrated the data within the IDL superset MIR developed for the Owens Valley Radio Observatory and adapted for the SMA (Scoville et al. 1993).[6] The imaging was performed in MIRIAD (Sault et al. 1995).

3. RESULTS AND ANALYSIS

3.1. 440 μm *Continuum Emission*

The spectra presented in Figure 1 exhibit many molecular lines; therefore, a continuum image had to be constructed with great care. The continuum image presented in Figure 3 (*right*) was constructed by averaging the part of the USB spectrum with no detectable line emission as shown in Figure 1. The corresponding apparently line-free part of the LSB is considerably smaller, and thus the comparable pseudocontinuum image is noisier. Although we therefore omit the LSB data for the scientific interpretation, we point out that the peak fluxes in the LSB continuum image vary by less than 10% compared to those in the USB image. This shows the good relative flux calibration between both sidebands.

Weak lines below the detection limit may contribute to the continuum emission. To estimate the contamination from such weak lines, we produced an additional pseudocontinuum data set of the LSB data including all spectral lines. We used the LSB data for this purpose because their line contamination is more severe. Fitting two point sources in the *u-v* domain (1) to the whole LSB continuum data and (2) to the apparently line-free LSB data (for details see § 3.1.1), the measured fluxes from step 1 were only $\sim$15% higher for source *I* and SMA1 than those from step 2. In our data, possible weak lines unidentified due to noise are on average less than 10% of the average peak flux of the strong lines (Fig. 1). Since the strong lines already cover about half of the given bandpass (Fig. 1), the contribution from possible weak lines below the detection limit amounts to only about 1.5%. This is negligible compared to the absolute flux uncertainties.

The derived 440 μm continuum emission map is shown in the right panel of Figure 3. To make a proper comparison with the 865 μm emission, we also show the original image at that wavelength (Beuther et al. 2004), as well as an image of the 865 μm observations using only the 30–160 kλ data range, which is the range of baselines sampled by our 440 μm data. In spite of strong sidelobes and the imaging problems described in § 2, the 440 μm map shows two distinct pointlike sources associated with source *I* and SMA1. Comparing this image with the 30–160 kλ image at 865 μm, we find at the longer wavelength similar structures for source *I* and SMA1 plus emission from the hot core. Additional features such as source *n* are not present in the 440 μm continuum image, likely because of the poor imaging capabilities and thus strong sidelobes of the observations (see § 2). The main difference between the 440 μm and the 865 μm continuum images is the strong presence of the hot core in the longer wavelength image, whereas we find only a small extension to the east in 440 μm. Imaging of the spectral line data in the 440 μm band (§ 3.2) shows that in spite of the mentioned imaging limitations (§ 2), we can spatially image and separate line emission from

[6] See also the MIR cookbook by Charlie Qi at http://cfa-www.harvard.edu/~cqi/mircook.html.

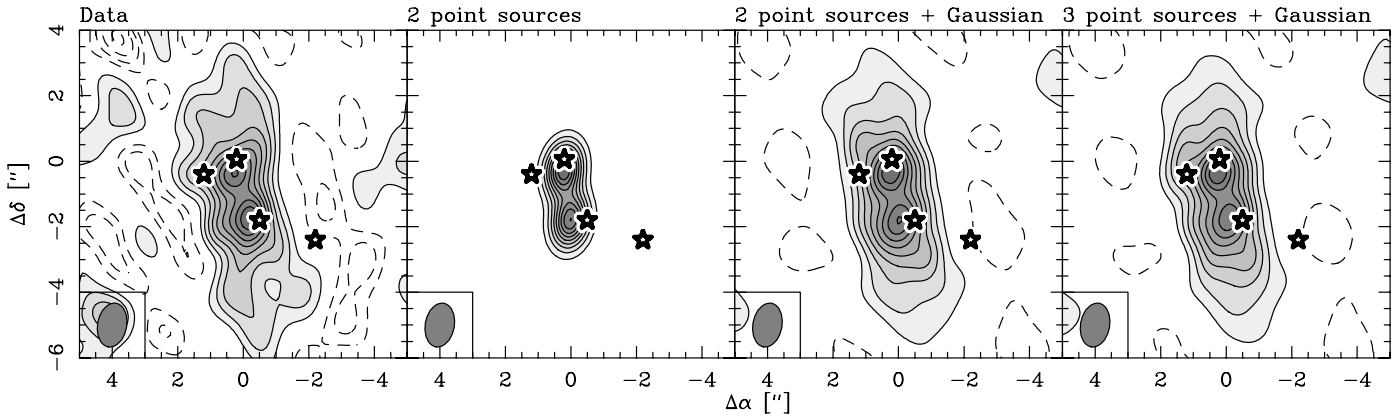

FIG. 4.—Original image and model fits to the 690 GHz continuum data. *Far left:* Original image; *near left:* two point sources model; *near right:* two point sources + Gaussian model; *far right:* three point sources + Gaussian model. The contouring is done in ±10% to ±90% steps from the peak emission of the four images. The peak values are 10.3, 7.7, 10.2, and 10.6 Jy from left to right, respectively. The stars again mark the sources identified in the left panel of Fig. 3. The synthesized beams are presented at the bottom left of each panel.

source *I* and the hot core. Hence, while it remains puzzling that the typically strong hot core is only barely detectable in our 440 μm image, it might be a real feature of the data indicating a peculiar low spectral index α of the hot core emission (for a detailed discussion see § 3.1.5).

3.1.1. *Flux Measurements*

The 440 μm continuum emission in Figure 3 gives the impression that the point sources *I* and SMA1 are embedded in a larger scale ridge emission. While Orion KL is known to be part of the large-scale Orion molecular ridge (e.g., Lis et al. 1998), the larger scale emission in our image is to some degree also an artifact of the data reduction, since we had to use clean boxes and thus shifted emission from the entire primary beam to the central region. Hence, flux measurements toward source *I* and SMA1 from the images will give values that are too high. To avoid these problems, we fitted the data in the *u-v* domain assuming

1. two point sources at the positions of source *I* and SMA1,
2. two point sources at the positions of source *I* and SMA1 + an elliptical Gaussian component,
3. three point sources at the positions of source *I*, SMA1, and the hot core peak,
4. three point sources at the positions of source *I*, SMA1, and the hot core peak + an elliptical Gaussian component.

Afterward, we imaged the models using exactly the same *u-v* coverage and imaging parameters employed previously for the real data. Figure 4 shows a direct comparison between the image of the original data and three model fits. We find that the models with an additional larger scale elliptical Gaussian component reproduce the data rather well. Although the fitted fluxes for source *I* and SMA1 vary by less than 15% (within the calibration uncertainty) with or without the third point source at the position of the hot core, the image of the three point sources + Gaussian model most resembles the original data image. Therefore, we use this model for the following analysis.

These simplified models allow us to bracket the fluxes from source *I*, SMA1, and the hot core (HC). The three-point-sources-only model likely overestimates the intrinsic fluxes because it adds some of the underlying large-scale emission to the point sources. Contrary to this model, the three point sources + Gaussian model underestimates the point-source contributions and thus the point-source fluxes. The measured values for both *u-v* fitting approaches are given in Table 1.

TABLE 1
MEASURED VALUES FOR BOTH *u-v* FITTING APPROACHES

SOURCE	FLUX (Jy)	
	Three Point Sources	Three Point Sources + Gaussian
I	7.9	4.6
SMA1	7.1	3.5
HC	3.1	2.4
Gaussian[a]	...	178

[a] Size is 6.″8 × 2.″7.

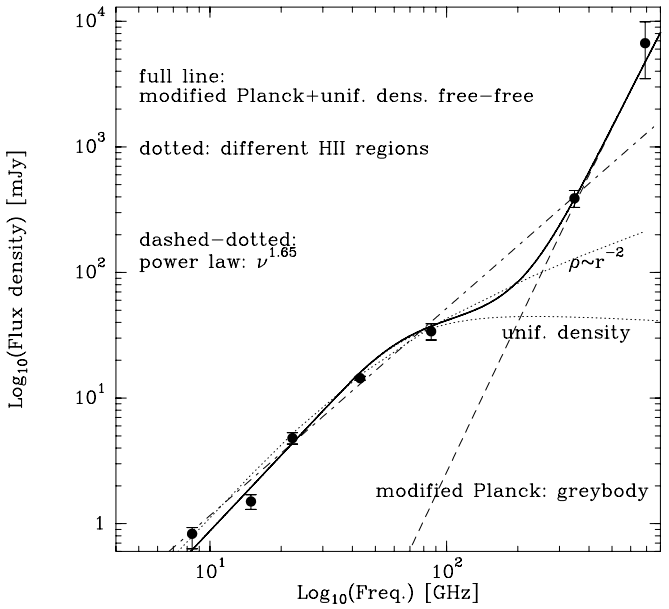

FIG. 5.—SED of source *I*. The measured fluxes are represented by filled circles with error bars, and the various lines show different attempts to fit the data as labeled within the plot. The 15, 22, and 86 GHz fluxes are taken from Plambeck et al. (1995 and references therein), the 8 and 43 GHz measurements are more recent values (consistent with the error bars of the previous measurements by Menten & Reid [1995; M. J. Reid et al. 2006, in preparation]), the 345 GHz data point is from Beuther et al. (2004), and the 690 GHz point is from this work.

TABLE 2
OBSERVED LINES

ν[a] (GHz)	Line[b]	E_u (K)	Δv[c] (km s^{-1})	Tentative[d]
679.781.....	$C^{33}S(14–13)$	247	7.1	...
679.831.....	$CH_3CN(37_3–36_3)$	688	8.3	...
679.895.....	$CH_3CN(37_2–36_2)$	649	8.3	...
679.934.....	$CH_3CN(37_1–36_1)$	628	13.4[e]	...
679.947.....	$CH_3CN(37_0–36_0)$	621	13.4[e]	...
680.210.....	UL	...	7.1	$C_2H_3CN(72_{4,69}–71_{4,68})$ at 680.211 GHz
	...	...	...	OCS(56–55) at 680.213 GHz
680.485.....	UL	...	13.8[e]	$C_2H_5CN(78_{4,75}–77_{4,74})$ at 680.481 GHz
680.500.....	UL	...	13.8[e]	$C_2H_5CN(78_{3,75}–77_{3,74})$ at 680.507 GHz
680.804.....	$CH_3OH(22_1–21_2)A^-$	606	12.6	...
680.890.....	$HNCO(31_{2,29}–30_{2,28})$	696	16.4	...
681.086.....	UL	...	4.8	$CH_3CN(37_7–36_7)v_8 = 1$ at 681.087 GHz
	...	...	...	$CH_3OCH_3(19_{6,13}–18_{5,14})$ at 681.090 GHz
681.150.....	UL	...	5.5	$C_2H_5OH(56_{21,35}–56_{21,35})$ at 681.152 GHz
681.218.....	UL	...	5.2	$CH_3CN(37_9–36_9)v_8 = 2$ at 681.216 GHz
	...	...	...	$C_2H_5CN(70_{8,63}–71_{3,68})$ at 681.224 GHz
681.263.....	UL	...	10.4	$HCOOCH_3(35_{8,28}–35_{4,31})$ at 681.265 GHz
	...	...	...	$SO_2(68_{9,59}–68_{8,60})$ at 681.266 GHz
	...	...	...	$^{33}SO(16–15)$ at 681.269 GHz
681.328.....	UL	...	6.3	$CH_3CN(37_1–36_1)v_8 = 2$ at 681.329 GHz
681.440.....	UL	...	8.6	$CH_3CN(37_5–36_5)v_8 = 1$ at 681.438 GHz
681.589.....	UL	...	8.7	$CH_3CN(37_7–36_7)v_8 = 2$ at 681.590 GHz
681.674.....	$SO_2(35_{3,33}–34_{2,32})$	598	11.4	...
681.733[f].....	UL	...	...	...
689.840.....	UL	...	5.2	$D_2CO(20_{2,18}–20_{2,19})$ at 689.840 GHz
	...	...	...	$C_2H_3CN(21_{6,15}–22_{4,18})$ at 689.842 GHz
	...	...	...	SiN(16–15) at 689.842 GHz
	...	...	...	$C_2H_5CN(28_{10,19}–27_{9,18})$ at 689.842 GHz
690.349.....	UL	...	7.0	...
690.551.....	$H^{13}CN(8–7)$	149	16.2	...
690.890.....	UL	...	6.0	$HCOOCH_3(27_{7,21}–26_{6,20})$ at 690.891 GHz
	...	...	...	$C_2H_3CN(72_{30,42}–71_{30,41})$ at 690.892 GHz
	...	...	...	$C_2H_5CN(23_{11,12}–22_{10,13})$ at 690.892 GHz
691.473.....	CO(6–5)	116	?[g]	...

[a] The frequency uncertainties are below 1 MHz, mostly even below 0.1 MHz. The frequencies for the unidentified lines are derived via setting $v_{lsr} = 5$ km s^{-1}.
[b] UL: unidentified line.
[c] FWHM of Gaussian fits to the vector-averaged spectra of the short 25 m baseline (see Fig. 1).
[d] Tentative molecular transition identifications, which are still very uncertain!
[e] Line blend.
[f] This line is at the edge of the bandpass and thus only partly detected. Therefore, the frequency is even more uncertain.
[g] Due to missing flux, a line fit does not make sense.

Including the 25% calibration uncertainty, the 440 μm flux measurements with conservative estimates of the error budget are

$$3.5 < S(I) < 9.9 \Rightarrow S(I) \sim 6.7 \pm 3.2 \text{ Jy},$$
$$2.6 < S(\text{SMA1}) < 8.9 \Rightarrow S(\text{SMA1}) \sim 5.75 \pm 3.15 \text{ Jy},$$
$$1.8 < S(\text{HC}) < 3.9 \Rightarrow S(\text{HC}) \sim 2.85 \pm 1.05 \text{ Jy}.$$

The errors are not to be understood as 1 or 3 σ values, but they instead give the extreme values of what the fluxes of the three sources could be. As outlined above, the line contamination of our continuum data set is very low.

3.1.2. *The Large-Scale Structure*

Obviously, from our data we cannot well constrain the large-scale flux distribution. However, the fitted 178 Jy is a lower limit to the large-scale flux, since we have no data below 28 kλ, and Johnstone & Bally (1999) measured a 450 μm single-dish peak flux of 490 Jy with the Submillimeter Common-User Bolometric Array (SCUBA) at 7.″5. Furthermore, we investigated the influence of a large source with a flux of a few hundred janskys on our observations. Modeling different source sizes and *observing* them with the given *u-v* coverage, the size scale of the large-scale emission has to exceed 11″. Larger sources are filtered out by the observations and do not distort the observed continuum image significantly, whereas smaller sources with large flux would completely dominate the observations. The scale of 11″ corresponds approximately to the size scales theoretically traceable by the shortest baselines of 28 kλ (corresponding to approximately 9″ scales).

3.1.3. *Source I*

Prior to these observations, the SED of source *I* could be fitted well by two very different models, as the result of either optically thick proton-electron free-free emission up to 100 GHz plus dust emission that accounts for most of the submillimeter flux, or H^- free-free emission that gives rise to a power-law spectrum with a power-law index of $\sim$1.6 (Beuther et al. 2004). Since the two models vary strongly at higher frequencies, an accurate 440 μm

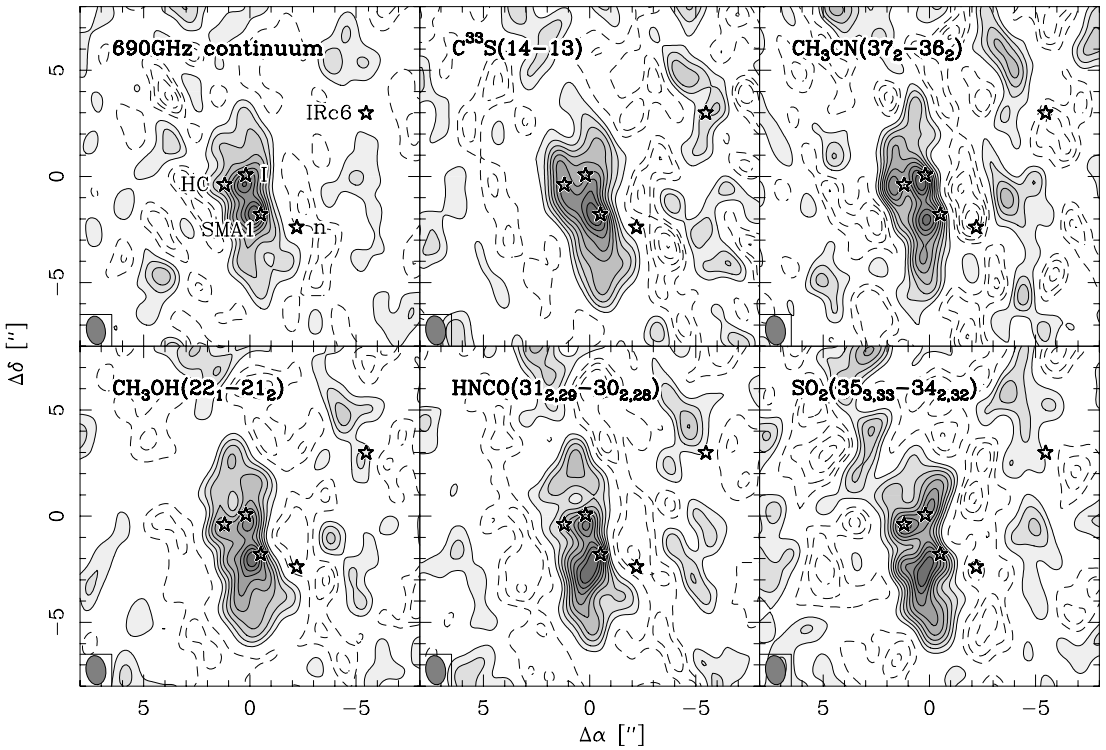

FIG. 6.—Integrated line emission maps after continuum subtraction. The top left panel again shows the continuum image as presented in Fig. 3 for comparison, and the other five panels show representative molecular line maps as labeled within each panel. Positive emission is presented in a gray scale and solid contours, and negative emission—due to missing short spacings—is shown in dashed contours. The contours range from 10% to 90% of the peak emission in each image. The synthesized beams are shown at the bottom left of each panel.

continuum flux measurement was of utmost importance in discriminating between these models.

Figure 5 shows the complete SED of source *I* from 8 to 690 GHz. The measured 690 GHz flux fits the model of a proton-electron free-free plus dust emission spectrum well, but not the model of the power-law spectrum expected for H^- free-free emission. Therefore, the 440 μm continuum data can discriminate between the two models, and the SED of source *I* turns out to be a rather typical SED for deeply embedded protostellar sources. One important result here is that the turnover frequency (i.e., the transition from optically thick to optically thin emission) is much higher in source *I* than in other protostars, in which it is typically in the range 10–40 GHz.

3.1.4. *SMA1*

The observations show that SMA1 is not just an extension of the hot core but is an independent protostellar source. Based on Plateau de Bure Interferometer (PdBI) $HC_3N(10–9)$ observations of vibrational excited lines, de Vicente et al. (2002) predicted an additional massive protostellar source in the region approximately 1.″8 south of source *I*, which is the location of SMA1. Only two flux measurements exist for SMA1: at 865 μm ($S \sim 0.36 \pm 0.07$ Jy; Beuther et al. 2004) and at 440 μm ($S \sim 5.75 \pm 3.15$ Jy). The spectral index between these two bands is $S \propto \nu^{\alpha}$ with $\alpha \sim 4.0^{+0.9}_{-1.4}$. In spite of the broad range of potential α, the data are consistent with a typical dust opacity index $\beta = \alpha - 2$ in star-forming regions of two. The nondetection of SMA1 at centimeter and infrared wavelengths suggests that it may be one of the youngest sources in the evolving cluster.

3.1.5. *The Hot Core*

The hot core flux values we derived above are probably more uncertain than those from source *I* and SMA1 because the hot core is only weakly discernible from the rest of the image in the original data, as well as in the model. Furthermore, the response of the continuum and line emission to the poor *u-v* sampling is not the same in interferometric studies, and we cannot entirely exclude that the weakness of the hot core in the 440 μm data is caused by this poor *u-v* sampling and the resulting imaging problems. Keeping in mind these uncertainties, we nevertheless can use the existing data to estimate a spectral index between the previous 865 μm measurement and these new data. The flux measurements in the two bands toward the hot core peak position [$S(865\,\mu\mathrm{m}) \sim 0.54 \pm 0.11$ Jy (Beuther et al. 2004) and $S(440\,\mu\mathrm{m}) \sim 2.85 \pm 1.05$ Jy] result in a range of potential spectral indices $S \propto \nu^{\alpha}$ with $\alpha \sim 2.4^{+0.8}_{-0.9}$. These values are considerably lower than for source *I* and SMA1.

Single-dish spectral index studies toward the Orion A molecular cloud qualitatively find a somewhat lower spectral index toward Orion KL than toward most of the rest of the Orion A molecular cloud (Lis et al. 1998; Johnstone & Bally 1999), but the two studies do not agree quantitatively. Lis et al. (1998) find a dust opacity index of $\beta \sim 1.8$ corresponding in the Rayleigh-Jeans limit to a spectral index of $\alpha \sim 3.8$, whereas Johnstone & Bally (1999) find a spectral index of $\alpha \sim 2.2$. Nevertheless, considering the large number of potential uncertainties (e.g., calibration, different beam sizes, and line contamination), the qualitatively lower spectral index α toward Orion KL compared with its surroundings appears to be a reliable result from the single-dish studies.

In contrast to source *I* and SMA1, for which the spectral indices are both consistent with typical values of α of $\sim$4 in star-forming regions, the lower spectral index toward the hot core is intriguing. Furthermore, lower resolution observations show that on larger spatial scales the data are dominated by the apparently more extended hot core emission (e.g., Plambeck et al. 1995;

Blake et al. 1996; Beuther et al. 2004). Therefore, the different spectral indices indicate that the lower single-dish spectral index may be due to hot core emission distributed over larger spacial scales, whereas the protostellar sources *I* and SMA1 exhibit spectral indices more typical of those from other star-forming regions.

3.2. *Spectral Line Emission*

We detected 24 spectral lines over the entire bandpass of 4 GHz (Fig. 1 and Table 2). This is a significantly lower line number than the $\sim$150 lines over the same spectral width at 348 GHz. The lower sensitivity of the 690 GHz data compared with the 345 GHz observations accounts for this difference to some degree. Furthermore, at 690 GHz each line of a given Δv covers twice the frequency range of that at 345 GHz, and thus strong lines dominate a broader part of the spectrum than at lower frequencies. Furthermore, to first order the observing frequency is proportional to the average energy levels of observable lines in that frequency range, and the lower number of line detections at 690 GHz indicates that the bulk of the gas is at lower temperatures (see temperature discussion in § 3.3). Nevertheless, the energy levels of the 690 GHz lines (Table 2) show that a very warm gas component has to be present in the region as well. Temperature estimates based on the $CH_3CN(37_K-36_K)$ are derived below (§ 3.3). Comparing these spectra with the single-dish spectra toward the same region (Schilke et al. 2001; Harris et al. 1995), we find a large number of lines previously not detected in this region. Line identifications were done first using the line survey by Schilke et al. (2001) and then cross-checking the identifications with the molecular databases at Jet Propulsion Laboratory (JPL) and the Cologne Database for Molecular Spectroscopy (CDMS; Poynter & Pickett 1985; Müller et al. 2001). It has to be noted that the unambiguous identification of spectral lines becomes more difficult at higher frequencies, which is discussed in § 3.4.

Table 2 also shows the line widths derived from Gaussian fits to the vector-averaged spectra on a short baseline of 25 m (Fig. 1). Since the measured line widths are associated with gas from the whole emission in the primary beam, they do not represent the line width toward a selected position but rather an average over the whole region. The derived values for Δv range between 4.8 and 16.4 km s^{-1}. We could not fit the CO(6–5) line due to the missing flux. While some of the broader line widths may be due to the outflows in the region, this is probably not the main reason for most of the lines, since the spectra often resemble a Gaussian profile. It seems more likely that different velocity components, as well as large intrinsic line widths toward each position due to turbulence and/or internal motion, cause a reasonable fraction of the line width. For a discussion of the CH_3CN line widths, see § 3.3.

Figure 6 presents the images of the velocity-integrated emission of a few of the identified molecular lines in the bandpass. As discussed in §§ 2 and 3.1, imaging of the emission turns out to be difficult, as evidenced by the strong negative sidelobes in Figure 6. Since our primary beam is rather small (18″) and the imaging gets worse toward the edge of the primary beam, we consider only emission at the centers of the maps to be reliable. All line images in Figure 6 show considerable emission toward source *I*, SMA1, and the hot core peak position. $C^{33}S(14–13)$ peaks toward SMA1 with lower level emission from the hot core and source *I*. In contrast, the line images from $CH_3CN(37_2–36_2)$, $CH_3OH(22_1–21_2)$, and $SO_2(35_{3,33}–34_{2,32})$ all show emission peaks from source *I*, SMA1, and the hot core peak position. The $HNCO(31_{2,29}–30_{2,28})$ image exhibits emission peaks associated with source *I* and SMA1 and only lower level emission from the hot core position. A striking difference between these 440 μm line images and our previous study in the 865 μm band (Beuther et al. 2005) is that the higher excited lines in the 440 μm band show line emission from source *I*. In the 865 μm band, we found mainly SiO emission from source *I*; other species appear to avoid the source in the lower frequency band. This indicates the presence of high temperatures in the close environment of source *I*.

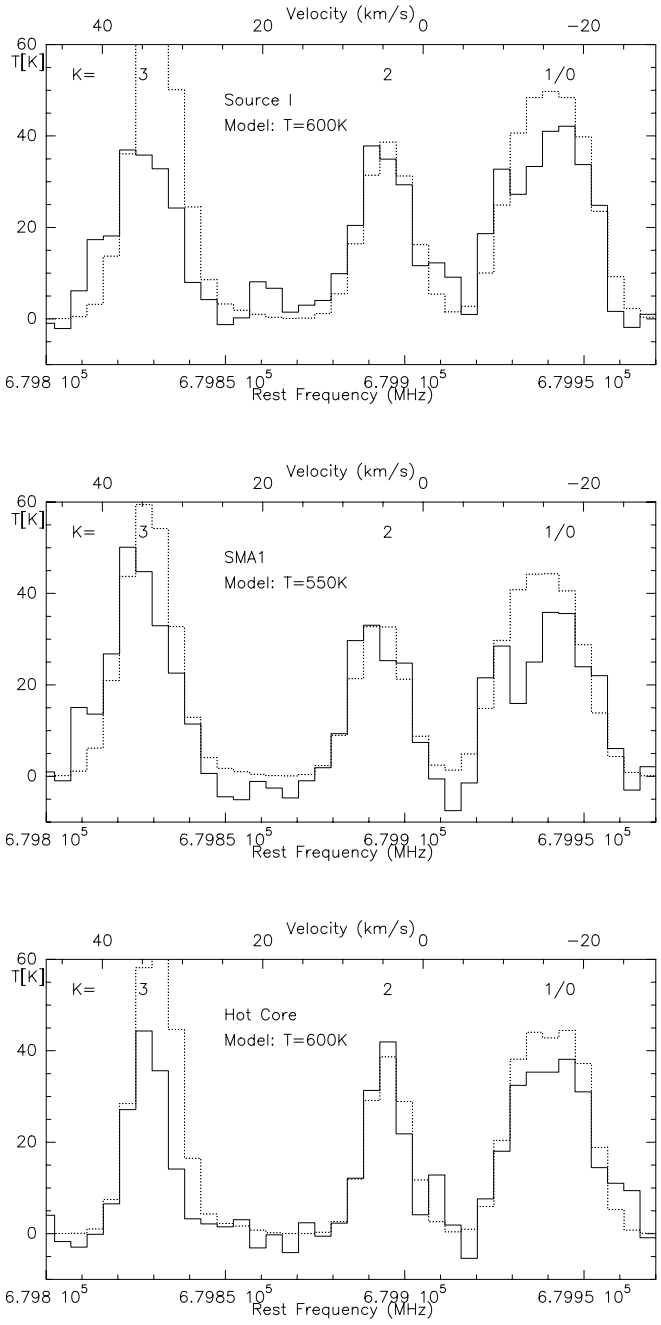

FIG. 7.—$CH_3CN(37_K–36_K)$ spectra taken toward the CH_3CN peak positions associated with source *I*, SMA1, and the hot core (see Fig. 6). The solid lines show the data, and the dotted lines show the LTE model spectra (adopted temperatures are given in each panel). The data are not very sensitive to the temperatures and can be modeled with *T* varying by approximately ±200 K.

We could not produce reliable emission maps for the CO(6–5) and $H^{13}CN(8–7)$ lines. While this is less of a surprise for CO, which is known to be extended and thus difficult to image interferometrically, $H^{13}CN$ was expected to be far more compact, comparable to many of the other imaged lines. However, comparing all lines in our frequency setup [excluding only the CO(6–5) line], the $H^{13}CN(8–7)$ line has one of the broadest line

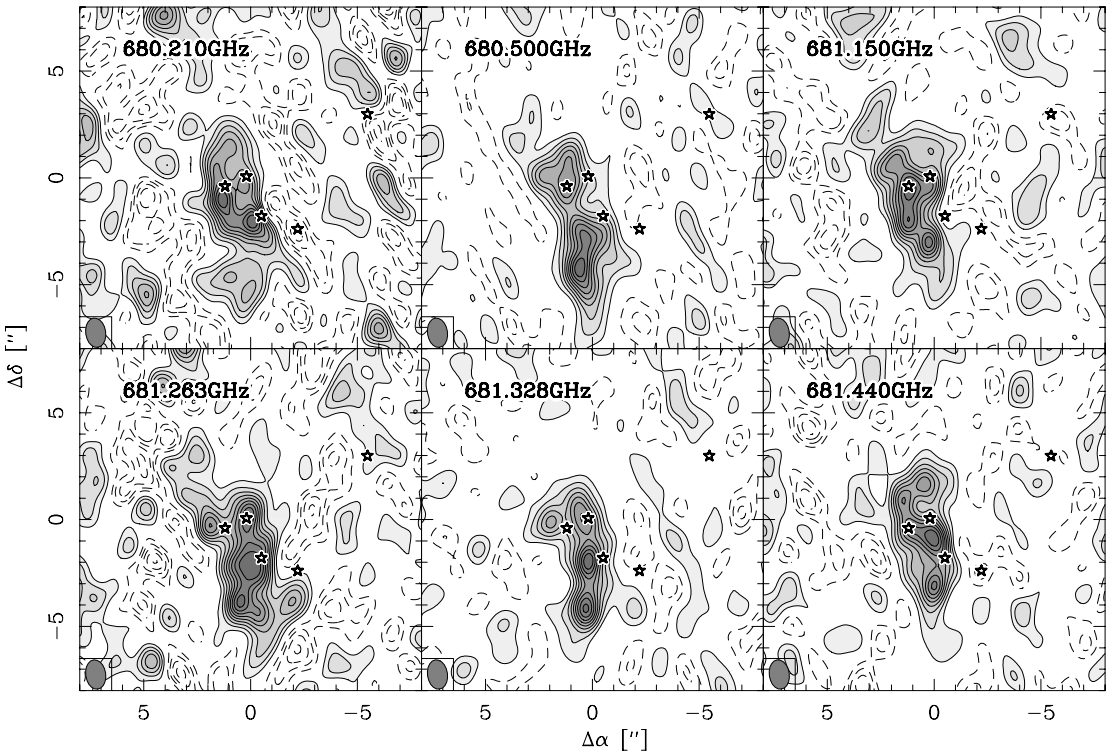

FIG. 8.—Integrated line emission maps of some unidentified lines after continuum subtraction; positive emission is presented in a gray scale and solid contours, and negative emission—due to missing short spacings—is shown in dashed contours. The contours range from 10% to 90% of the peak emission in each image. The rest frequency for each line set to $v_{lsr} = 5$ km s^{-1} is shown at the top left of each map. The symbols are the same as in the previous figures, and the synthesized beams are shown at the bottom left of each panel.

widths ($\Delta v \sim 16.2$ km s^{-1}) and thus may be more strongly affected by the molecular outflows present than initially expected. This could explain our inability to properly image the $H^{13}CN(8–7)$ emission.

3.3. $CH_3CN(37_K–36_K)$: *Temperature Estimates and Line Widths*

Since we observed the $K = 0$, 1, 2, and 3 lines of the $CH_3CN(37_K–36_K)$ lines (the $K = 0$ and 1 lines are blended), we can use this K series for temperature estimates of the warm gas component in the regions. Figures 6 and 7 show the integrated $CH_3CN(37_2–36_2)$ emission map and spectra of all K-components toward the CH_3CN peak positions associated with source I, SMA1, and the hot core.

Using the XCLASS superset to the CLASS software (P. Schilke 2005, private communication), we produced model spectra in local thermodynamic equilibrium (Fig. 7). This software package uses the line catalogs from JPL and CDMS (Poynter & Pickett 1985; Müller et al. 2001). Because the $K = 3$ component has double the statistical weight of the $K = 0$, 1, and 2 lines, one expects in the optically thin case larger line intensities for the $K = 3$ transition. Toward all three positions, the modeled $K = 3$ intensity is larger than observed, indicating relatively high optical depths. The upper energy levels E_u of the various K-ladder lines range only between 621 and 685 K (Table 2), and the data are not very sensitive to the temperature. We find reasonable model spectra in the 600 K regime with a large potential range of temperatures of ±200 K. The CH_3CN model column densities we used are of the order of a few times 10^{16} cm^{-2}, and the line width adopted for the modeling was 7.0 km s^{-1} for source I and SMA1 and 6 km s^{-1} for the hot core. In spite of the large error bars, the temperatures traced by these high-energy lines are, as expected, higher than the highest temperatures of 350 K previously derived from our CH_3OH multiline analysis in the 865 μm band (Beuther et al. 2005). We attribute this temperature difference mainly to the various gas components at different temperatures and densities and to the different excitation energies of the spectral lines in the 690 and 337 GHz bands.

Furthermore, we can compare the modeled $CH_3CN(37_K–36_K)$ line widths of the order of 6–7 km s^{-1} with the previous SMA observations of the $CH_3CN(19_8–18_8)$ line at 348 GHz (Beuther et al. 2005). The measured $CH_3CN(19_8–18_8)$ from SMA1 and the hot core are 4.6 and 4.1 km s^{-1}, respectively. Beuther et al. (2005) found only very weak $CH_3CN(19_8–18_8)$ toward source I. Although the excitation temperatures E_u of the $CH_3CN(37_2–36_2)$ and the $CH_3CN(19_8–18_8)$ lines are approximately the same (649 and 624 K, respectively), it is interesting that the line width toward the $CH_3CN(37_2–36_2)$ is larger. Since the critical densities between the $CH_3CN(37_K–36_K)$ and $CH_3CN(19_K–18_K)$ series vary by about 1 order of magnitude ($\sim 10^8$ and $\sim 10^7$ cm^{-3}, respectively), this indicates that the higher density gas $CH_3CN(37_K–36_K)$ lines are likely subject to significantly more turbulent motions. As already pointed out by Sutton et al. (1986), radiative excitation is unlikely to significantly affect the populations of the vibrational ground state transitions, even for high J levels.

3.4. *Unidentified Lines (ULs)*

Fourteen out of the 24 detected spectral lines remain unidentified or only tentatively identified. Such a high percentage of unidentified lines (~58%) has rarely been reported, to our knowledge only recently toward Sgr B2 (Friedel et al. 2004). The previous single-dish line surveys of Orion KL report percentages of unidentified lines between 8% and 15% (Schilke et al. 1997, 2001; Comito et al. 2005). Orion KL is known to have a number of

different velocity components approximately between 2 and 9 km s^{-1} (e.g., Genzel & Stutzki 1989), and we cannot determine at which velocity an unidentified line is beforehand. Hence, at 690 GHz the frequency range of potential molecular lines between 2 and 9 km s^{-1} is 16 MHz, compared to 8 MHz at 345 GHz [$\Delta\nu = \Delta v(\nu/c)$]. Furthermore, going to higher frequencies, astronomical spectral line studies are rare, and identifications that rely only on laboratory work are difficult. Hence, identifying spectral lines gets more complicated at higher frequencies.

Figure 8 presents some of the integrated line emission maps of the ULs. Since these lines are on average of lower intensity, the signal-to-noise ratio in the maps is worse than for the identified lines in Figure 6. The rest frequencies listed for the ULs in Table 2 (and shown in Fig. 8) correspond to the lines being set to a $v_{\rm lsr}$ of 5 km s^{-1}, implying the potential range of frequencies for each line as discussed above. In principle, it should sometimes be possible to associate ULs with molecular families (e.g., oxygen-, nitrogen-, or sulphur-bearing species) based on the spatial distribution of the gas (see, e.g., the previous 865 μm Orion line studies by Beuther et al. 2005). However, since the quality of the images is rather poor, this is a difficult task for this data set. Nevertheless, we tried to associate some ULs with potential molecular transitions. Table 2 lists a few tentative candidate lines for the ULs, which, however, are only suggestions and not real identifications.

4. DISCUSSION AND CONCLUSIONS

The presented line and continuum data of Orion KL in the 440 μm/690 GHz band show the power of high spatial resolution studies in the submillimeter wavelength bands. The measured continuum flux from source *I* allows us to differentiate between various previously proposed physical models. Source *I* appears to be a rather "normal" protostellar object with a SED fitted by a two-component model of proton-electron free-free emission below 100 GHz plus a dust component contributing to the flux in the submillimeter bands. Furthermore, the source SMA1 becomes more prominent at higher frequencies and is clearly distinguishable from the hot core emission. Since SMA1 is detected neither at centimeter nor at infrared wavelengths, it may be one of the youngest sources in the evolving cluster. The only weak detection of the hot core at 440 μm is puzzling. Although it might be a real feature of the new high spatial resolution 440 μm continuum data, we cannot entirely exclude that it is caused by the poor *u*-*v* sampling and resulting imaging problems. Keeping the uncertainties in mind, we find a lower spectral index toward the hot core compared with those toward source *I* and SMA1. This is consistent with lower spectral indices found toward Orion KL in lower spatial resolution single-dish observations that are dominated by the hot core emission.

The spectral line maps trace a warm gas component at the center of the region, mainly confined to source *I*, SMA1, and the hot core peak position. Temperature estimates based on the $CH_3CN(37_K–36_K)$ *K*-ladder ($K = 0, \ldots, 3$) lines indicate a warm gas component in the regime of 600 ± 200 K. The number of unidentified lines in the given setup is large. Potential reasons are discussed, of which the two main ones are likely the large potential spread in velocity, and thus frequency, of the unidentified lines and the less explored submillimeter wavelength band.

We would like to thank Peter Schilke for providing the XCLASS software to model the CH_3CN spectra. We also thank Darek Lis for discussing spectral indices in Orion KL. We also appreciate the helpful comments from the referee. H. B. acknowledges financial support by the Emmy-Noether-Program of the Deutsche Forschungsgemeinschaft (DFG, grant BE2578/1).

REFERENCES

Allen, D. A., & Burton, M. G. 1993, Nature, 363, 54
Beuther, H., et al. 2004, ApJ, 616, L31
———. 2005, ApJ, 632, 355
Blake, G. A., Mundy, L. G., Carlstrom, J. E., Padin, S., Scott, S. L., Scoville, N. Z., & Woody, D. P. 1996, ApJ, 472, L49
Chernin, L. M., & Wright, M. C. H. 1996, ApJ, 467, 676
Chrysostomou, A., Burton, M. G., Axon, D. J., Brand, P. W. J. L., Hough, J. H., Bland-Hawthorn, J., & Geballe, T. R. 1997, MNRAS, 289, 605
Comito, C., Schilke, P., Phillips, T. G., Lis, D. C., Motte, F., & Mehringer, D. 2005, ApJS, 156, 127
de Vicente, P., Martín-Pintado, J., Neri, R., & Rodríguez-Franco, A. 2002, ApJ, 574, L163
Dougados, C., Lena, P., Ridgway, S. T., Christou, J. C., & Probst, R. G. 1993, ApJ, 406, 112
Friedel, D. N., Snyder, L. E., Turner, B. E., & Remijan, A. 2004, ApJ, 600, 234
Genzel, R., & Stutzki, J. 1989, ARA&A, 27, 41
Gezari, D. Y., Backman, D. E., & Werner, M. W. 1998, ApJ, 509, 283
Greenhill, L. J., Gezari, D. Y., Danchi, W. C., Najita, J., Monnier, J. D., & Tuthill, P. G. 2004, ApJ, 605, L57
Gurwell, M. A. 2004, ApJ, 616, L7
Gurwell, M. A., & Muhleman, D. O. 1995, Icarus, 117, 375
———. 2000, Icarus, 145, 653
Harris, A. I., Avery, L. W., Schuster, K.-F., Tacconi, L. J., & Genzel, R. 1995, ApJ, 446, L85
Ho, P. T. P., Moran, J. M., & Lo, K. Y. 2004, ApJ, 616, L1
Johnstone, D., & Bally, J. 1999, ApJ, 510, L49
Lis, D. C., Serabyn, E., Keene, J., Dowell, C. D., Benford, D. J., Phillips, T. G., Hunter, T. R., & Wang, N. 1998, ApJ, 509, 299
Liu, S., Girart, J. M., Remijan, A., & Snyder, L. E. 2002, ApJ, 576, 255
Masson, C. R. 1994, in IAU Colloq. 140, Astronomy with Millimeter and Submillimeter Wave Interferometry, ed. M. Ishiguro & J. Welch (ASP Conf. Ser. 59; San Francisco: ASP), 87
Menten, K. M., & Reid, M. J. 1995, ApJ, 445, L157
Müller, H. S. P., Thorwirth, S., Roth, D. A., & Winnewisser, G. 2001, A&A, 370, L49
Plambeck, R. L., Wright, M. C. H., Mundy, L. G., & Looney, L. W. 1995, ApJ, 455, L189
Poynter, R. L., & Pickett, H. M. 1985, Appl. Opt., 24, 2235
Sault, R. J., Teuben, P. J., & Wright, M. C. H. 1995, in ASP Conf. Ser. 77, Astronomical Data Analysis Software and Systems IV, ed. R. A. Shaw, H. E. Payne, & J. J. E. Hayes (San Francisco: ASP), 433
Schilke, P., Benford, D. J., Hunter, T. R., Lis, D. C., & Phillips, T. G. 2001, ApJS, 132, 281
Schilke, P., Groesbeck, T. D., Blake, G. A., & Phillips, T. G. 1997, ApJS, 108, 301
Schultz, A. S. B., Colgan, S. W. J., Erickson, E. F., Kaufman, M. J., Hollenbach, D. J., O'dell, C. R., Young, E. T., & Chen, H. 1999, ApJ, 511, 282
Scoville, N. Z., Carlstrom, J. E., Chandler, C. J., Phillips, J. A., Scott, S. L., Tilanus, R. P. J., & Wang, Z. 1993, PASP, 105, 1482
Shuping, R. Y., Morris, M., & Bally, J. 2004, AJ, 128, 363
Stolovy, S. R., et al. 1998, ApJ, 492, L151
Sutton, E. C., Blake, G. A., Genzel, R., Masson, C. R., & Phillips, T. G. 1986, ApJ, 311, 921
Wilner, D. J., Wright, M. C. H., & Plambeck, R. L. 1994, ApJ, 422, 642
Wilson, T. L., Gaume, R. A., Gensheimer, P., & Johnston, K. J. 2000, ApJ, 538, 665
Wright, M. C. H., Plambeck, R. L., & Wilner, D. J. 1996, ApJ, 469, 216